

Solid-state eutectic electrolyte via solvation regulation for voltage-elevated and deep-reversible Zn batteries

Received: 28 August 2024

Accepted: 15 May 2025

Published online: 26 May 2025

Wei Ling^{1,2}, Funian Mo³, Xiongwei Wu², Xianxiang Zeng^{1,2}, Jian Xiong⁴ & Yan Huang¹✉

Solid-state electrolytes have the great potential to achieve high-voltage and durable zinc-based batteries, but their effectiveness is limited by inferior ionic conductivity and large interfacial voltage polarization. Here, a nonflammable solid-state eutectic electrolyte is prepared in situ by cross-linking polymerization of ternary eutectic electrolyte with ethoxylated trimethylpropane triacrylate. Thanks to the intermolecular interaction among the deep eutectic solvents and polymer skeleton, the solid-state eutectic electrolyte possesses satisfactory room-temperature ionic conductivity of $3.94 \times 10^{-3} \text{ S cm}^{-1}$. It enables the symmetric batteries with 80% Zn utilization operating stably at high current density of 8.0 mA cm^{-2} for 1700 h, exceeding all non-aqueous and most aqueous zinc batteries. More importantly, due to solvation structure regulation, the solid-state eutectic electrolyte is found to elevate discharge voltage plateau to 2.1 V in Zn full batteries, and presents favorable rate performance and cyclic stability at $25 \pm 1^\circ \text{C}$.

As promising alternatives of conventional lithium-ion batteries, Zn-based batteries have attracted much attention due to their low cost, intrinsic safety and eco-friendliness nature^{1–3}. However, their voltage as well as reversibility of Zn electrode under high depth of discharge, are critical bottlenecks for practical application. Solid-state electrolytes with wide voltage window guarantee high-voltage Zn-based batteries as well as effectively alleviate dendrite growth and low coulombic efficiency caused by side reactions^{4–6}. Nevertheless, they typically exhibit low ionic conductivity and poor interfacial compatibility, leading to severe discharge voltage drop of full batteries, especially under the condition of high zinc utilization and large current density^{7–10}. More importantly, they have never been found to elevate voltage plateau of batteries under the condition of given positive and negative electrodes. Although several works reported a high discharge plateau of above 2.0 V, they relied on the selection of high-potential positive electrodes and/or low-potential negative electrodes instead of the electrolyte effect^{11–15}. So far, solid-state Zn-based batteries rarely

exhibit discharge voltage plateau of over 1.9 V, and are difficult to cycle at zinc utilization of over 50% and current density of over 5.0 mA cm^{-2} .

Among various solid-state electrolytes, the solid-state eutectic electrolyte exhibits advantages of relatively high ionic conductivity, safety and good thermal/chemical stability^{16–23}. Unfortunately, it still shows non-ideal ionic conductivity (below $10^{-3} \text{ S cm}^{-1}$) and low zinc ion mobility number (0.2–0.3) at 25°C , which is mainly attributed to high viscosity of eutectic electrolytes and easy mobility of deep-eutectic solvents^{24–27}.

Here, we reported a nonflammable solid-state eutectic electrolyte (PSNE) via in situ thermal polymerization of ternary eutectic electrolyte with ethoxylated trimethylpropane triacrylate (ETPTA) (Fig. 1a). Benefiting from the intermolecular interaction of the ternary eutectic electrolyte, the ionic conductivity of PSNE at 25°C breaks through to $3.94 \times 10^{-3} \text{ S cm}^{-1}$. Due to the anchoring effect of polymer skeleton on the solvent molecules, the symmetric batteries using PSNE maintain durable lifetime of 1700 h at 8.0 mA cm^{-2} under 80% Zn utilization,

¹Sauvage Laboratory for Smart Materials, School of Materials Science and Engineering, Harbin Institute of Technology, Shenzhen 518055, PR China. ²School of Chemistry and Materials Science, Hunan Agricultural University, Changsha 410128, PR China. ³School of Future Technology, Shenzhen Technology University, Shenzhen 518055, PR China. ⁴Center for Composite Materials and Structures, Harbin Institute of Technology, Harbin 150080, PR China.

✉ e-mail: yanhuanglib@hit.edu.cn

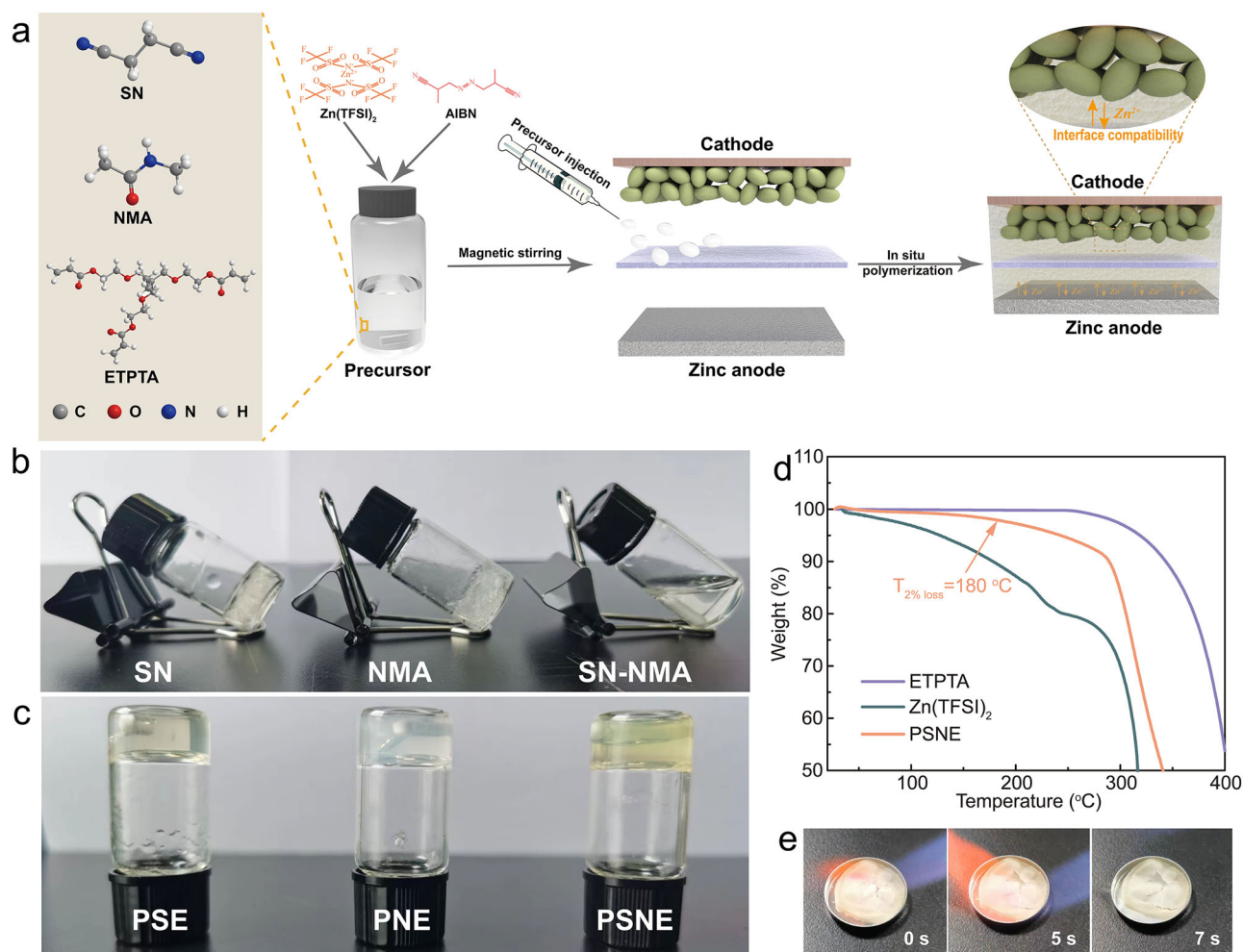


Fig. 1 | Preparation and thermal performance of the solid-state eutectic electrolyte. a Schematic diagram of eutectic electrolyte via in situ polymerization. Photograph showing **b** different solvent components and **c** corresponding solid-

state eutectic electrolytes. **d** Thermogravimetric analysis ($T_{2\% \text{ loss}}$ represents the temperature at which the mass loss reaches 2%) and **e** non-flammability test of PSNE.

suprassing all non-aqueous and most aqueous zinc batteries. Furthermore, derived from the solvation structure regulation, the solid-state eutectic electrolyte elevates the discharge voltage plateau (up to 2.1 V) of Zn batteries and the plateau elevation is universal in different positive electrodes. Thus, we overturn the classical cognition regarding the voltage of batteries and realize deep charging/discharging.

Results

Preparation of the solid-state eutectic electrolyte

As shown in Fig. 1b, single butanedinitrile (SN) or N-methylacetamide (NMA) presented a solid state at around 25°C , but their mixture was transformed into a liquid state. This is attributed to the fact that the strong intermolecular force between SN and NMA can lower the melting point of the mixture, thus forming a eutectic solvent that helps the dissolution and dissociation of zinc salts. After addition of zinc bis(trifluoromethanesulfonyl)imide ($\text{Zn}(\text{TFSI})_2$) (0.5 M), they formed different liquid eutectic electrolytes, named as SE, NE and SNE, respectively, indicating that strong intermolecular forces among $\text{Zn}(\text{TFSI})_2$, SN and NMA can further lower the melting point of these mixtures (Supplementary Fig. 1). Finally, ETPTA and azodiisobutyronitrile (AIBN) serving as monomer and initiator, respectively, were added to eutectic electrolytes above, followed by curing in a high-temperature oven to form solid-state eutectic electrolytes, named as PSE, PNE and PSNE, respectively (Fig. 1c).

As we know, the thermal stability of electrolyte is critical to the practical application of zinc metal batteries (ZMBs). The thermogravimetric test (TGA) curve in Fig. 1d show that PSNE loses only 2% of its original weight at 180°C , suggesting a good thermal stability. Furthermore, PSNE cannot be ignited in contact with the flame for several seconds, demonstrating low vapor pressure and non-flammability (Fig. 1e). Compared with conventional aqueous electrolytes, PSNE not only retains the high safety of Zn-based batteries, but also solves the problem of solvent evaporation from the electrolytes.

Composition and mechanism analysis of the solid-state eutectic electrolyte

The ionic conductivity of solid-state eutectic electrolyte is closely related to the relative content of zinc salt. The alternating current (AC) impedance spectra of solid eutectic electrolytes with different zinc salt contents are shown in Supplementary Fig. 2, where PSNE-1, PSNE-3, PSNE-5, PSNE-7 and PSNE-10 were assigned to the $\text{Zn}(\text{TFSI})_2$ concentration of 0.1 mol L^{-1} , 0.3 mol L^{-1} , 0.5 mol L^{-1} , 0.7 mol L^{-1} and 1.0 mol L^{-1} in the precursor solution, respectively. The thickness (d) and area (S) of the tested electrolytes were 0.3 cm and 0.785 cm^2 , respectively, thus the ionic conductivity of solid-state eutectic electrolytes with different zinc salt contents can be calculated by the equation ($\sigma = d/RS$). As shown in Fig. 2a, the solid-state eutectic electrolyte can obtain the highest ionic conductivity of $3.94 \times 10^{-3} \text{ S cm}^{-1}$ at

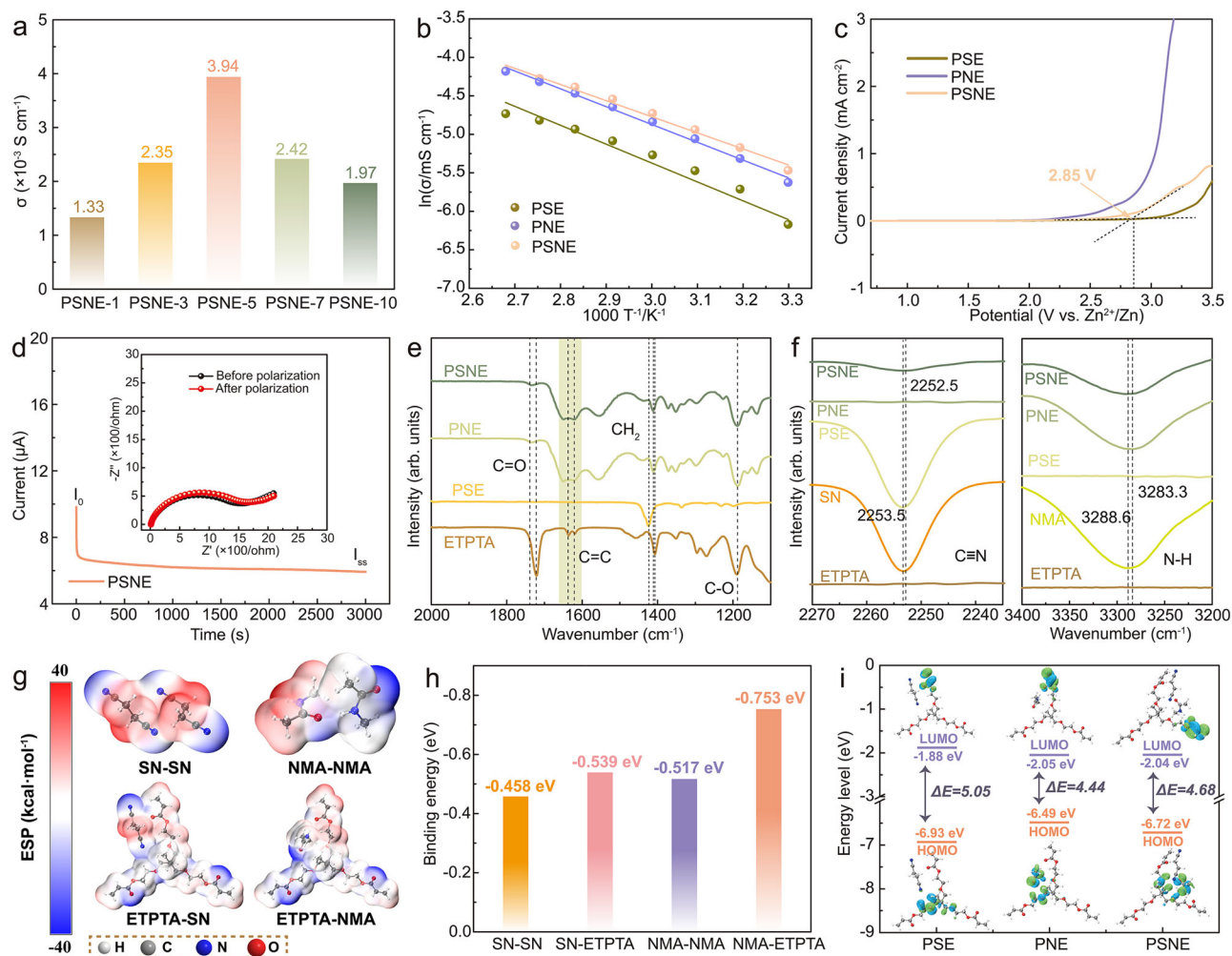


Fig. 2 | Electrochemical performance and mechanism analysis of the solid-state eutectic electrolyte. a Ionic conductivities of PSNE with different contents of $\text{Zn}(\text{TFSI})_2$ at 25 °C. **b** Arrhenius plots of different solid-state electrolytes. **c** Linear sweep voltammetry of different solid-state electrolytes at 1.0 mV s^{-1} under temperature of 25 °C. **d** Direct-current polarization and EIS variation of Zn PSNE Zn

symmetrical batteries at 25 °C (applied voltage: 10 mV; i_0 : initial current; i_{ss} : steady-state current). **e, f** FTIR spectra of solid-state eutectic electrolytes. **g** Electrostatic potential and **h** binding energy of various components. **i** Molecular orbital energy level of PSN, PNE, and PSNE.

$\text{Zn}(\text{TFSI})_2$ content of 0.5 mol L^{-1} under a temperature of 25 °C. As shown in Supplementary Fig. 3, PSNE still possessed a room-temperature ionic conductivity of $3.37 \times 10^{-3} \text{ S cm}^{-1}$ via 50 times of bending, which was 85.5% of the initial ionic conductivity, indicating relatively good mechanical stability. In addition, the differences in electrochemical properties between PSN, PNE and PSNE solid-state electrolytes were investigated. Supplementary Fig. 4 represents their AC impedance spectra at different temperatures. Thus, the ionic conductivity of the solid-state electrolytes at different temperatures can be obtained (Supplementary Table S1). Compared to PSN and PNE, PSNE exhibited the highest ionic conductivity at each temperature, and the ionic conductivity of PNE was much higher than that of PSN. This is attributed to the role of NMA to decrease the viscosity of electrolyte as well as the interaction between SN and NMA to form a low eutectic solvent, which promote the dissociation of $\text{Zn}(\text{TFSI})_2$. Meanwhile, based on the Arrhenius relationship plots ($\sigma = A \exp(-E_a/RT)$) (Fig. 2b), the activation energies of PSN, PNE and PSNE are 0.22 eV, 0.20 eV and 0.18 eV, respectively, indicating an improved ion conduction property of PSNE.

In addition to the ionic conductivity, a wide voltage window is also one of the important properties of solid-state electrolytes. As the linear voltammetric curves (LSV) shown in Fig. 2c, PSNE possessed an

oxidation potential of 2.85 V, which was higher than that of PNE (2.5 V) and lower than that of PSE (3.2 V), suggesting that the addition of SN can effectively improve the antioxidant ability of the solid-state electrolyte. For comparing PSE with PSNE, the difference is because the SN content in PSE (88.4 wt%) is significantly higher than that in PSNE (8.5 wt%). Besides, the Zn^{2+} transfer number in solid state electrolytes has an important influence on the space charge layer effect and dendrite formation on the electrode surface. For this reason, the Zn Zn symmetric batteries was tested by direct-current polarization method, and the Zn^{2+} transfer number can be calculated by the following equation:

$$t^+ = \frac{i_{ss}(\Delta V - i_0 R_0)}{(i_0(\Delta V - i_{ss} R_{ss}))} \quad (1)$$

where t^+ represents Zn^{2+} transfer number, i_0 and i_{ss} express the current (A) before and after polarization, R_0 and R_{ss} are the impedance (Ω) before and after polarization, ΔV is the applied voltage (V). As shown in Fig. 2d, PSNE exhibited Zn^{2+} transfer number of 0.60, which is much higher than that of conventional liquid electrolytes (<0.3). For comparison, a liquid eutectic electrolyte (SNE) without ETPTA monomer possessed a Zn^{2+} transfer number of only 0.22 (Supplementary Fig. 5).

It is attributed to that the solid electrolyte has a higher binding effect for anions, thus promoting the migration of Zn^{2+} .

In order to analyze the composition and intermolecular interaction of solid electrolytes, Fourier infrared spectroscopy (FTIR) was performed for different solid electrolytes and monomers. As shown in Fig. 2e, the ETPTA monomer shows a characteristic absorption peak at 1630 cm^{-1} , which is attributed to the vibration of the $\text{C}=\text{C}$ bond²⁸, while the disappearance of this characteristic peak for the PSE, PNE and PSNE indicates the successful polymerization of ETPTA at high temperature. Moreover, the positions of characteristic peaks of $\text{C}=\text{O}$, CH_2 , $\text{C}\equiv\text{N}$ and N-H in the solid eutectic electrolytes were shifted to some extent compared with those of monomer, pure SN and NMA (Fig. 2f), suggesting that there are some interactions between the polymer backbone and SN/NMA, which facilitate the anchoring of solvent molecules on the polymer backbone and thus promote ionic conduction in the solid-state electrolytes. On this basis, Raman spectroscopy was used to analyze the interaction of $\text{Zn}(\text{TFSI})_2$ with SN and NMA. As shown in Supplementary Fig. 6 and Supplementary Note 1, the Raman characteristic peaks at 1238 cm^{-1} and 1130 cm^{-1} were attributed to CF_3 stretching and SO_2 vibrations in $\text{Zn}(\text{TFSI})_2$ ⁵. After the addition of SN and NMA, these peaks of the eutectic electrolyte (whether polymerized or unpolymerized) were relatively displaced, indicating that there are interaction forces among $\text{Zn}(\text{TFSI})_2$, SN and NMA. In addition, compared with the smaller change of the $\text{C}\equiv\text{N}$ position of SN in the eutectic electrolytes, the displacement of the $\text{C}=\text{O}$ characteristic peak of NMA in the eutectic electrolytes was more obvious, which demonstrates the interaction force between $\text{Zn}(\text{TFSI})_2$ and NMA is stronger than that of SN, suggesting that NMA was easier to dissociate $\text{Zn}(\text{TFSI})_2$.

Density Functional Theory (DFT) was used to probe the interactions among components within the solid-state eutectic electrolytes, and the theoretical calculations were all performed based on the Gaussian 16 series program²⁹. First, the electrostatic potentials of the different components and their interactions were calculated to show the electronegativity and positively charged groups on these components and the polymer backbone, which mainly contribute to intermolecular coordination (Fig. 2g, Supplementary Fig. 7, Supplementary Fig. 8, Supplementary Fig. 9 and Supplementary Data 1). These interactions mainly involved Van der Waals intermolecular force, hydrogen bond and ion-dipole interaction. As shown in Fig. 2h, the binding energies of SN-SN, NMA-NMA, and SN-NMA solvent molecules themselves are -0.458 eV , -0.517 eV , and -0.287 eV , respectively, suggesting a strong interaction among eutectic solvents. In contrast, the binding energies of polymer matrix-solvent molecule were increased to -0.539 eV (ETPTA-SN) and -0.753 eV (ETPTA-NMA), respectively, which was attributed to that SN and NMA tend to have stronger interactions with highly electronegative groups in ETPTA rather than their own dipole-dipole interaction. Furthermore, the binding energies of SN-NMA-ETPTA and SN-NMA-ETPTA-TFSI were increased to -1.566 eV and -1.409 eV , respectively (Supplementary Fig. 9f and Supplementary Fig. 9h). Such stronger interactions of polymer skeleton for SN and NMA is conducive to the anchoring of solvent molecules on the polymer skeleton, thus promoting ion conduction and stabilizing zinc electrode by reducing the decomposition of solvent molecules effectively.

To investigate the effect of intermolecular interactions on the stable voltage window of solid-state eutectic electrolytes, the molecular orbital energy levels of different systems were calculated, where the highest occupied molecular orbital (HOMO) and lowest unoccupied molecular orbital (LUMO) energy levels correspond to the oxidation and reduction potentials of the systems, respectively. As shown in Fig. 2i, compared with PNE (4.44 eV), PSE and PSNE displayed larger energy band widths of 5.05 eV and 4.68 eV , respectively, suggesting the addition of SN can effectively broaden the stable voltage window of solid-state electrolytes. In particular, the HOMO energy levels of PSE

and PSNE were -6.93 eV and -6.72 eV , respectively, being lower than that of PNE (-6.49 eV) (Supplementary Data 1). The lower HOMO reflects that it is more difficult for external oxidizing species to extract electrons from the electrolyte, because the electrons in the electrolyte are more tightly bound. This makes the electrolyte more stable in oxidative environments, thus enhancing its antioxidant ability. Thus, the DFT result verifies SN can enhance the antioxidant potential of solid-state electrolytes, which is consistent with the previous LSV data (Fig. 2c).

Stripping/plating reversibility of Zn electrode based on the solid-state eutectic electrolyte

In our previous work, ZnSnF@Zn was shown to be effective in improving the Zn plating/stripping performance of zinc electrode in aqueous electrolytes³⁰. Based on that, the zinc deposition behavior of ZnSnF@Zn in these solid-state eutectic electrolytes was further investigated. For this purpose, Pure Zn and ZnSnF@Zn were assembled into symmetric batteries with PSNE electrolyte, respectively. As shown in Supplementary Fig. 10, the symmetric battery based on PSNE electrolyte can run stably for 4000 h regardless of using Pure Zn or ZnSnF@Zn at a current density of 1.0 mA cm^{-2} , and their cycle lives are much longer than that of most zinc electrodes in aqueous electrolytes (below 2000 h)^{31–33}, confirming that solid-state eutectic electrolyte is able to significantly improve the zinc deposition behavior. In addition, compared with Pure Zn, ZnSnF@Zn based on PSNE always maintained a stable and smaller overpotential ($20\text{--}30\text{ mV}$) during long-term Zn plating/stripping, indicating an improved interfacial compatibility between solid-state eutectic electrolyte and ZnSnF@Zn electrode. ZnSnF@Zn|PSNE|Ti batteries were assembled to test their cyclic voltammetry, which exhibited small changes in peak current and peak potential during 80 cycles, suggesting the highly reversible electrochemical reaction process of ZnSnF@Zn in the presence of PSNE (Supplementary Fig. 11). Due to the favorable zinc deposition behavior of ZnSnF@Zn in PSNE, subsequent studies on the electrochemical performance of PSNE were mainly based on ZnSnF@Zn .

To investigate the effect of PSNE on zinc deposition efficiency, the asymmetric ZnSnF@Zn|Cu batteries were assembled and tested for long cycle. As shown in Fig. 3a, the ZnSnF@Zn|PSNE|Cu can maintain an average coulombic efficiency of 99.86% during 1100 cycles at 1.0 mA cm^{-2} and 1.0 mAh cm^{-2} . By contrast, ZnSnF@Zn|PNE|Cu possessed an average coulombic efficiency of only 95.43% with 250 cycles, and ZnSnF@Zn|PSE|Cu exhibited very fluctuating deposition efficiency within less than 100 cycles, which results from the lowest ionic conductivity of PSE with large interfacial impedance. In addition, the ZnSnF@Zn|PSE|Cu showed a low first zinc deposition efficiency of 43.6%, which was much lower than that for ZnSnF@Zn|PNE|Cu (93.4%) and ZnSnF@Zn|PSNE|Cu (94.1%) (Supplementary Fig. 12). As shown in Supplementary Fig. 13, the solid-state electrolyte still possessed an intact structure after long-term Zn plating/stripping.

Besides, different solid-state electrolytes were assembled into ZnSnF@Zn|ZnSnF@Zn symmetric batteries, and the Zn plating/stripping performance at 80% zinc utilization was tested. Due to low ionic conductivity and large interfacial impedance, PSE-based symmetric batteries cannot operate normally at different current densities, indicating inferior zinc deposition behavior (Supplementary Fig. 14). The current density of PNE-based symmetric batteries can reach 5.0 mA cm^{-2} at 80% zinc utilization, and the battery was short-circuited when the current density rised to 8.0 mA cm^{-2} . By comparison, the symmetric battery based on PSNE always showed stable Zn plating/stripping during the total running time of 352 h, and its overpotential increased slowly with the increase of current density from 1.0 mA cm^{-2} to 10.0 mA cm^{-2} (Fig. 3b). When the densities returned to the initial current density, the overpotential can still return to the initial level, showing the high rate performance of the zinc deposition in PSNE. In addition to rate performance, long cycle stability is also important for

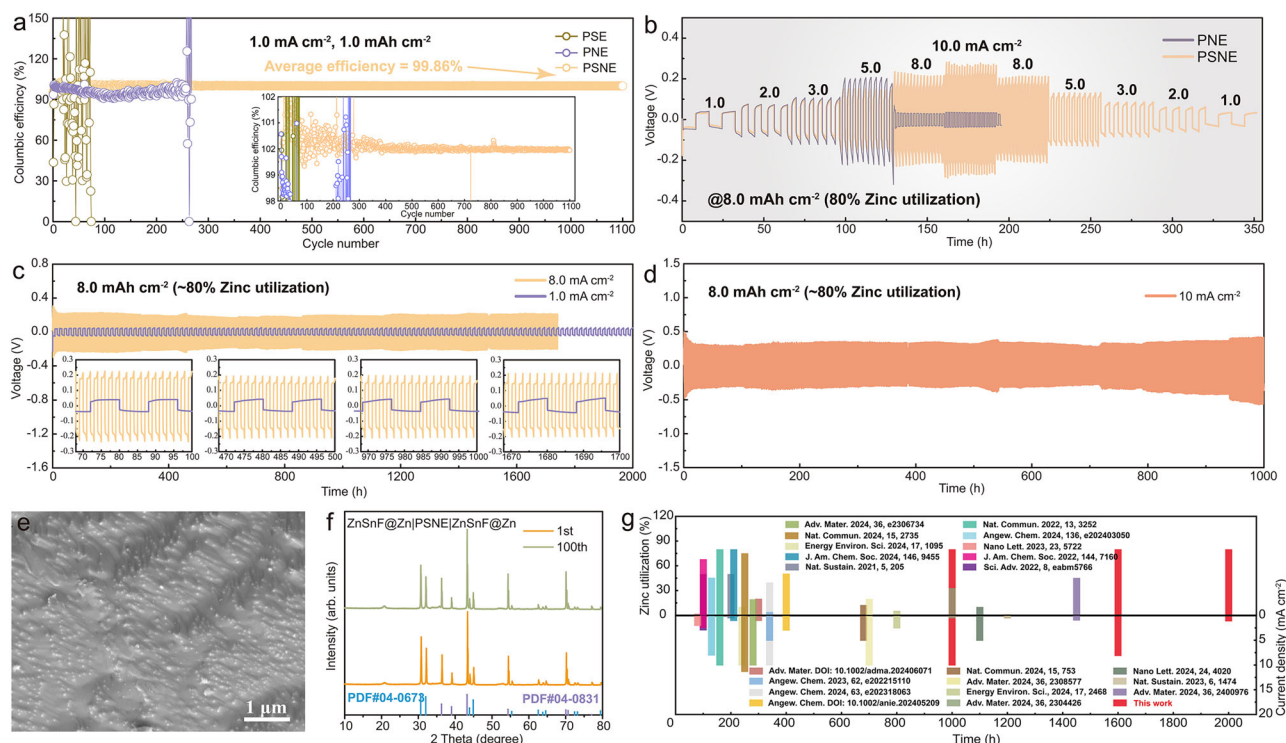


Fig. 3 | Effects of the solid-state eutectic electrolyte on the Zn metal deposition behavior at 25±1 °C. a Zn plating/stripping performance of ZnSnF@Zn||Cu batteries with different solid-state electrolytes. The inset in Fig. 3a shows an enlarged view of coulombic efficiency for Zn deposition. **b** Rate performance of symmetric batteries with zinc utilization of 80%. **c, d** Long-term Zn plating/stripping

performance of symmetric batteries with PSNE at 80% zinc utilization. **e** SEM image of ZnSnF@Zn with 80% zinc utilization after 100 cycles at 10 mA cm⁻² and 8.0 mAh cm⁻². **f** XRD patterns of ZnSnF@Zn with 80% zinc utilization after 1 and 100 cycles at 10 mA cm⁻² and 8.0 mAh cm⁻². **g** Comparison of zinc utilization, cycle life and current density between this work and recent literatures^{31,32,55-73}.

zinc electrode. As shown in Fig. 3c, at 1.0 mA cm⁻², the symmetrical battery based on PSNE can run stably for 2000 h under 80% zinc utilization, and its overpotential was slightly changed from the initial 45.9 mV to 45.7 mV after Zn plating/stripping. When the current density is increased to 8.0 mA cm⁻², the symmetric battery can maintain a stable cycle for 1700 h, and the overpotential was always stable at about 200 mV during the long cycle. Even at the current density of 10 mA cm⁻², the symmetric battery still displayed a stable operation for 1000 h (Fig. 3d). These results confirmed that PSNE can greatly improve the stability of Zn plating/stripping for zinc electrode under the harsh conditions of high zinc utilization and high current density.

To investigate further the effect of PSNE on the zinc deposition behavior, the morphology of zinc electrode after plating/stripping was characterized. As shown in Fig. 3e and Supplementary Fig. 15, the zinc electrode showed a flat surface morphology and no fragmented structures in the cross section. In order to evaluate the effect of PSNE on the suppression of side reactions, XRD tests were performed on the cycled zinc electrode. As shown in Fig. 3f, after 1 and 100 cycles in PSNE, ZnSnF@Zn exhibited the same characteristic diffraction peaks as before plating/stripping, mainly attributed to Sn (PDF#04-0673) and Zn (PDF#04-0831). Similarly, for the Pure Zn electrode, the characteristic diffraction peaks were the same as those before plating/stripping without heterophase peaks (Supplementary Fig. 16), suggesting that PSNE effectively suppresses the side reactions of zinc electrode. To evaluate the corrosion resistance of the Zn electrode in PSNE, the PSNE-based symmetric battery was tested by alternating cycles of zinc metal deposition/stripping (100 h) and resting (100 h). As shown in Supplementary Fig. 17, after each 100 h of resting, the symmetric battery could return to its original stable working condition, and its average overpotential was stable at about 45 mV during long-term plating/stripping of 1100 h. The favorable performance recovery of the symmetrical battery is attributed to the fact that PSNE

can effectively inhibit the corrosion of zinc electrode, thus avoiding the undesirable self-discharge phenomenon of the battery. Compared with the performance reported in the literature, the symmetric battery based on PSNE presents great advantages in the stability of Zn plating/stripping under the harsh conditions of high zinc utilization rate and high current density, surpassing the plating/stripping performance of zinc electrode in all non-aqueous electrolytes and most aqueous electrolytes reported so far (Fig. 3g). Specific performance parameters were shown in Supplementary Table S2.

Performance of solid-state full batteries

Based on the wide voltage window and reversible zinc deposition behavior, the applicability of PSNE was analyzed and evaluated in the high-voltage ZMBs. First, K_{1.6}Mn_{1.2}Fe(CN)₆ (MnHCF), a Prussian blue analogue, was selected as the high-voltage positive electrode and assembled with PSNE and ZnSnF@Zn to form a solid-state ZMB³⁴. As shown in Supplementary Fig. 18, the characteristic diffraction peaks of the prepared MnHCF corresponded to the standard PDF card (PDF#51-1896). Subsequently, CV tests were performed to analyze the electrochemical process of the solid-state ZMBs. Figure 4a shows the CV curves of ZnSnF@Zn|PSNE|MnHCF full battery in the scan rate range of 0.1–1.0 mV s⁻¹. Meanwhile, the log(*i*)-log(*v*) relationship between current and scan rate in Fig. 4b can reflect the charge storage behavior during charging and discharging, based on the following equation:

$$i = av^b \quad (2)$$

where *i* represents specific current (A g⁻¹), *v* expresses scan rate (mV s⁻¹), *a* and *b* are adjustable parameter. The *b*-values corresponding to the redox peaks of A1, A2, C1, and C2 were calculated to be 0.57, 0.53, 0.54, and 0.52, respectively. These *b*-values were close to 0.5, indicating that the corresponding redox reactions were mainly controlled by diffusion

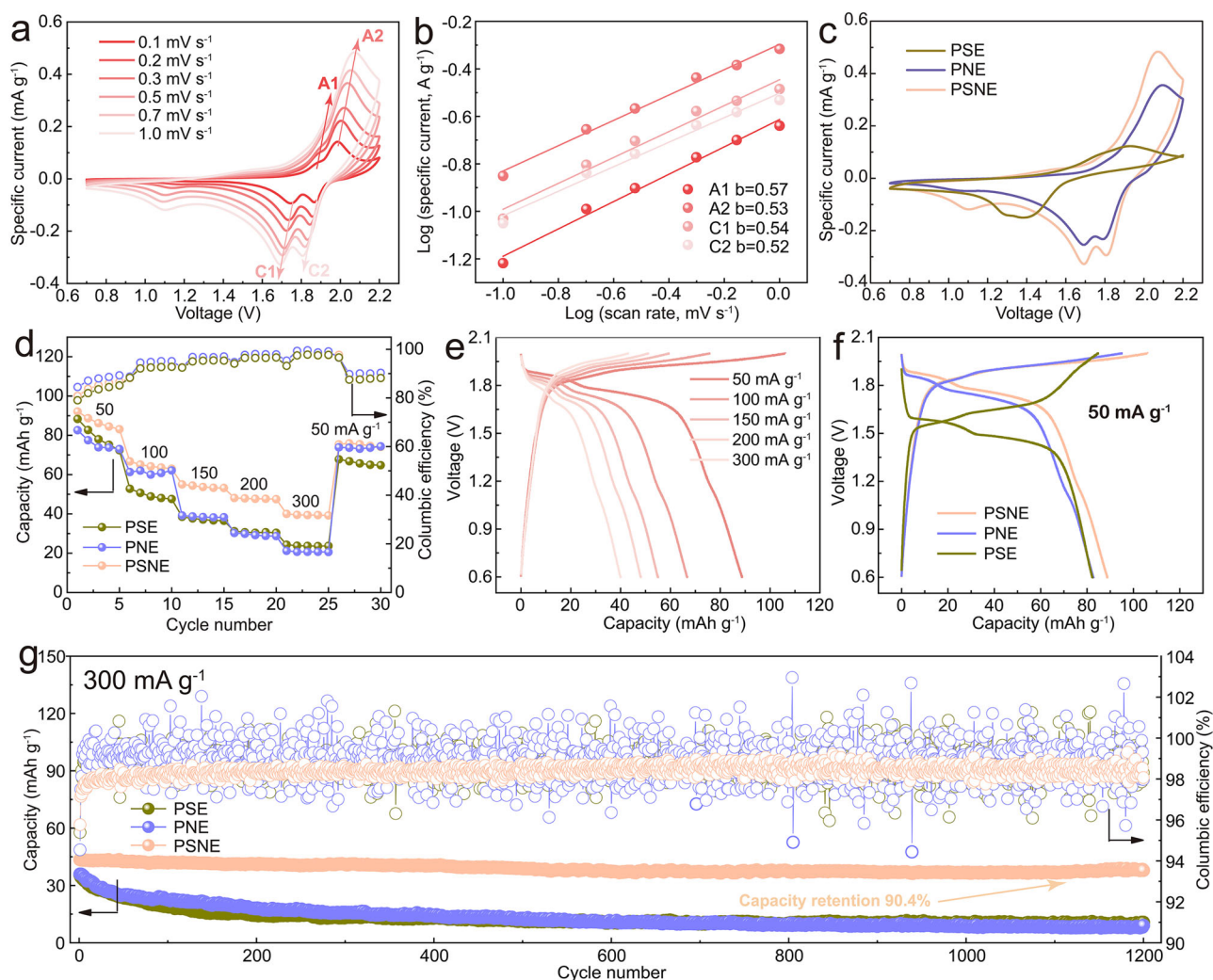


Fig. 4 | Electrochemical performance of ZnSnF@Zn|PSNE|MnHCF full batteries at 25±1 °C. a CV curves at various scan rate, **b** $\log(i)$ - $\log(v)$ plots and **c** CV comparison of ZnSnF@Zn|PSNE|MnHCF full batteries. **d** Rate performance, **e** GCD

curves based on PSNE, **f** GCD curves comparison and **g** long cycling performance of full batteries based on different solid-state electrolytes.

reactions. As shown in Fig. 4c, comparing the CVs of full batteries based on different electrolytes, it can be found that the ZnSnF@Zn|PSNE|MnHCF batteries had higher redox potentials and lower electrochemical polarization, which mainly stemmed from the good reversibility of Zn deposition and the effective reduction of interfacial reaction polarization promoted by PSNE.

Besides, the charge and discharge test of ZnSnF@Zn|PSNE|MnHCF full batteries was carried out. As shown in Fig. 4d, e, compared with PSE and PNE, PSNE-based full batteries possessed the best rate performance. At the specific current of 50 mA g⁻¹, PSNE-based full battery showed the highest discharge voltage plateau (average voltage greater than 1.6 V) and specific capacity of 88.7 mAh g⁻¹, suggesting that PSNE can contribute to high redox potential and reduce the polarization of charge and discharge process (Fig. 4f). In addition, under the specific current of 300 mA g⁻¹, the PSNE based full batteries still maintained a capacity retention of 90.4% after 1200 cycles (Fig. 4g), while the full batteries based on PSE and PNE possessed capacity retention of only 30.1% and 25.3%, respectively, fully confirming that PSNE can effectively improve the cycling stability of the high-voltage ZMBs.

Furthermore, the Na-Zn dual-ion solid-state battery was introduced to further evaluate the applicability of PSNE in higher voltage full-batteries. To realize the assembly of dual-ion batteries, 1.0 mol L⁻¹

sodium bis (trifluoromethylsulfonyl) imide (NaTFSI) was added when preparing the precursor solution of electrolytes such as PSNE. The schematic illustration of Zn|PSNE|NVPOF full batteries is shown in Fig. 5a. The positive reaction was based on the insertion and removal of Na⁺ in the positive electrode, while the negative reaction was based on the deposition and stripping process of zinc electrode. Here, Na₃V₂(PO₄)₂O₂F (NVPOF) was selected as positive electrode due to its high redox potential and relatively smooth voltage plateau of Na⁺ intercalating and deintercalating. As shown in Supplementary Fig. 19, the characteristic diffraction peaks of the prepared NVPOF corresponded with the standard PDF card (PDF#89-8485). Supplementary Fig. 20a displays the multi-sweep CV curves of Zn|PSNE|NVPOF full batteries, and two pairs of redox peaks (A1/C1 and A2/C2) appeared at all scan rates, corresponding to the insertion and removal processes of Na⁺ in NVPOF, respectively. The lower redox peak represents the redox process of V³⁺ and V⁴⁺, while the upper redox peak is due to the redox process of V⁴⁺ and V⁵⁺. In addition, the charge storage behavior can be reflected by the $\log(i)$ - $\log(v)$ relationship between current and scan rate. As calculated above (Eq. 2), it can be seen that the b values corresponding to the redox peaks of A1, A2, C1 and C2 are 0.58, 0.75, 0.57, and 0.72, respectively, indicating that the electrochemical reaction process is also mainly controlled by diffusion reaction (Supplementary Fig. 20b). As illustrated in Supplementary Fig. 21, the capacitive

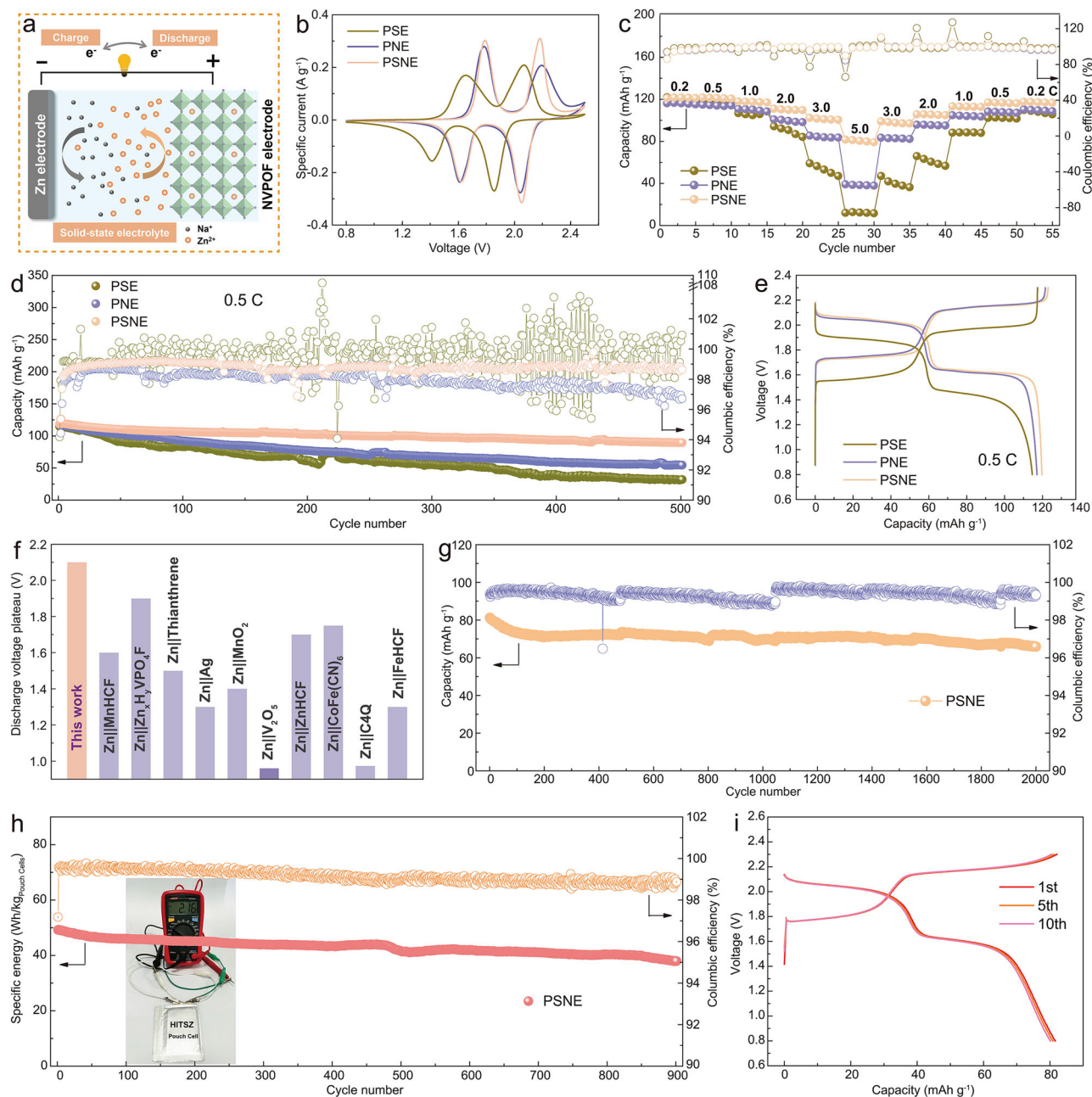


Fig. 5 | Electrochemical performance of Zn|PSNE|NVPOF full batteries at $25 \pm 1^\circ\text{C}$. **a** Schematic illustration of Zn|PSNE|NVPOF full batteries. **b** CV based on different electrolytes at 0.2 mV s^{-1} . **c** Rate-cycling of Zn|NVPOF with different electrolytes. **d** Cycling performance and **e** GCD curves of full batteries at 0.5 C . **f** Comparison of the discharge voltage plateau achieved in this work to various

reported zinc-based batteries^{36–45} **g** Cycling performance of ZnSnF@Zn|PSNE|NVPOF full battery at 5.0 C . **h** The entire specific energy stability of pouch batteries at 1.0 C (inset: photograph of measuring open-circuit voltage), and **i** corresponding charge and discharge curves.

contribution accounted for 35.2% of the total stored charge at 0.1 mV s^{-1} , which progressively increased to 63.1% as the scan rate increased to 1 mV s^{-1} . Supplementary Fig. 22 shows the long-cycling CV curves of ZnSnF@Zn|PSNE|NVPOF full batteries which maintained a good stability. In addition, by comparing CV of all batteries based on different electrolytes (Fig. 5b), it can be found that ZnSnF@Zn|PSNE|NVPOF batteries had the highest redox potential and lowest electrochemical polarization, which is the same as that of ZnSnF@Zn|MnHCF battery system.

As shown in Fig. 5c, the PSE- and PNE-based ZnSnF@Zn|NVPOF full batteries possessed discharge capacities of 121.9 and 116.2 mAh g^{-1} at 0.2 C ($1\text{ C} = 128\text{ mA g}^{-1}$), respectively, and only 38.4 and 12.3 mAh g^{-1} when the specific current rose to 5.0 C , respectively. In contrast, the

PSNE-based ZnSnF@Zn|NVPOF full batteries exhibited a discharge specific capacity of 121.2 mAh g^{-1} at 0.2 C . When the specific current increased to 5.0 C , ZnSnF@Zn|PSNE|NVPOF had a discharge capacity of 81.6 mAh g^{-1} , and can still recover to 117.6 mAh g^{-1} when the specific current returned to 0.2 C , showing a high rate-cycling performance (Supplementary Fig. 23). This is again mainly attributed to the high ionic conductivity of PSNE and the good interfacial compatibility between PSNE and positive/negative electrodes, as well as the wide voltage window to enhance the cycling stability of high-voltage full batteries.

In addition, the long cycle performance of ZnSnF@Zn|NVPOF full batteries based on different electrolytes was tested. As shown in Fig. 5d, at the low rate of 0.5 C , PSE and PNE-based ZnSnF@Zn|NVPOF

full batteries delivered specific capacities of 31.6 mAh g^{-1} and 54.5 mAh g^{-1} after 500 cycles, respectively, and the corresponding capacity retention was 27.5% and 46.3%. By contrast, ZnSnF@Zn|NVPOF full battery based on PSNE still possessed a high specific capacity of 89.6 mAh g^{-1} after 500 cycles, and its capacity retention can reach 75.7%. As shown in Supplementary Fig. 24, the Zn|PSNE|NVPOF full batteries exhibited small changes in impedance values after 100 cycles, suggesting a good cycling stability. Moreover, it can be seen from the comparison of the charge and discharge curves that $\text{ZnSnF@Zn|PSNE|NVPOF}$ full battery had two highest discharge voltage plateaus (1.7 V and 2.1 V) at 0.5 C, so that the average discharge voltage can reach 1.9 V (Fig. 5e). Compared with all ZMBs reported in the literature^{36–45}, our $\text{ZnSnF@Zn|PSNE|NVPOF}$ full batteries displayed a significant advantage in the discharge voltage plateau (2.1 V) (Fig. 5f). Moreover, contrast with commercial trimethyl phosphate electrolyte (TMP), the $\text{ZnSnF@Zn|PSNE|NVPOF}$ full batteries also possessed obvious advantages in terms of discharge voltage plateaus and rate performance, further verifying the superiority of the PSNE electrolyte (Supplementary Fig. 25). These further proved that PSNE can promote the high redox potential and reduce the polarization of charge and discharge process. Furthermore, at a large rate of 5.0 C, $\text{ZnSnF@Zn|PSNE|NVPOF}$ full battery had an initial capacity of 81.2 mAh g^{-1} , and retained a capacity retention of 81.2% after 2000 cycles (Fig. 5g). Under the same conditions, the specific capacity of the full batteries based on PSE and PNE were only 2.0 mAh g^{-1} and 19.7 mAh g^{-1} after 2000 cycles, and the capacity retention were only 27.1% and 58.9%, respectively (Supplementary Fig. 26). It is shown that PSNE can greatly improve the long cycle stability of solid-state high voltage batteries under the conditions of high-rate charging and discharging.

To further verify the practicability of PSNE, the $\text{ZnSnF@Zn|PSNE|NVPOF}$ pouch batteries were assembled via in-situ polymerization. As shown in Fig. 5h, the pouch batteries possessed an open-circuit voltage of 2.16 V, suggesting a discharge capability of high voltage. In addition, the pouch batteries (area: $5.3 \text{ cm} \times 4.2 \text{ cm}$, mass loading of positive electrode active material: 2.4 mg cm^{-2} , thickness of zinc metal electrode: $20 \text{ }\mu\text{m}$) exhibited overall specific energy of 50 Wh kg^{-1} , and still retained a retention of over 80% after 900 cycles. Figure 5i shows that the GCD curves of pouch batteries during the first ten cycles present a good overlap, indicating long cycle stability in terms of capacity, overall specific energy and discharge voltage.

Mechanism analysis for the voltage elevation of zinc batteries

To deeply understand the mechanism of PSNE to promote discharge voltage plateau of ZMBs, the solvation structures of SE, NE and SNE were analyzed via molecular dynamics simulation (MD). Figure 6a–c shows the snapshots of different eutectic electrolyte systems. According to the statistical diagram of this coordination number, the number of Zn^{2+} coordination TFSI in the three systems is mainly 2, and the number of SN coordination is mainly 2 in the first system (Fig. 6d–f). The second system is basically the same as the third system, and the coordination number of NMA is mainly 2 and 3, meanwhile, there is basically no coordination of SN in the third system. It can be known that the SN is hardly involved in the Zn^{2+} solvation structure in the PSNE electrolyte, which is mainly attributed to that the Zn^{2+} has a stronger coordination ability with NMA than SN^{46} . This can be interpreted that the amide group from NMA belongs to the strong polar solvent, and the coordination ability is significantly stronger than nitrile from SN.

Combining the previous GCD curves shown in Figs. 4f and 5e, PNE and PSNE both can enhance the charging and discharging voltage plateau of the full batteries, which should be attributed to the effect of NMA on Zn^{2+} solvation structure. Based on the above analysis, the main coordination structure in the above systems can be obtained (Supplementary Fig. 27 and Supplementary Data 1). Considering that the usual coordination number of Zn^{2+} is 4⁴⁷, the Zn^{2+} solvation structure in

SE, NE or SNE, are well established as $(\text{SN})_2\text{Zn}(\text{TFSI})_2$ and $(\text{NMA})_2\text{Zn}(\text{TFSI})_2$, respectively. Therefore, the coordination structure of Zn^{2+} in the two cases was optimized, and the structures are shown in Supplementary Fig. 28.

Based on classical mechanisms of electrochemical energy storage^{48,49}, the potential of positive electrode can be determined by Gibbs free energy difference (ΔG) between desolvation energy ($-\Delta E_1$) and intercalation energy (ΔE_2) ($\Delta G = \Delta E_2 - \Delta E_1$) (Supplementary Fig. 29). According to the Nernst equation ($\varepsilon = -\Delta G/nF$), the interfacial electrode potential is correlated with the ion's desolvation energy and intercalation energy. The intercalation energy of zinc ions remains fixed for a given electrode. Therefore, the total electrode potential is determined by the sum of the electrode charge transfer potential and the desolvation potential. Similarly, for a specific positive electrode, the charge transfer potential is a fixed value. Thus, the high desolvation energy barrier may prompt the electrode reaction potential. Based on above two structures, the desolvation process of Zn^{2+} was calculated by DFT. Figure 6g, h demonstrated the diagram of the energy barriers (kcal/mol) during the step-by-step desolvation process of $(\text{SN})_2\text{Zn}(\text{TFSI})_2$ and $(\text{NMA})_2\text{Zn}(\text{TFSI})_2$, respectively. Through the comparison between SE and NE in desolvation process, $(\text{SN})_2\text{Zn}(\text{TFSI})_2$ exhibited a total energy barrier of 513.47 kcal/mol, which was lower than that of $(\text{NMA})_2\text{Zn}(\text{TFSI})_2$ (529.51 kcal/mol). The electrode reaction potential consists of desolvation potential and insertion potential, and the higher energy barrier of Zn^{2+} desolvation can prompt electrode reaction potential because insertion potential of cations didn't change toward the same electrode material. Moreover, the higher desolvation energy barrier does not necessarily indicate slow ion transports because the Zn^{2+} ionic conductivity represents the ability of ions to transport within the electrolyte. Thus, as to the analysis above, the reason of voltage-increase of ZMBs using PNE and PSNE is mainly attributed to the fact that the addition of NMA can elevate Zn^{2+} desolvation potential, contributing to a higher discharging voltage plateau than that of PSE.

Discussion

In summary, we elevate the voltage plateau of Zn batteries by solid-state eutectic electrolyte to regulate the solvation structure of Zn^{2+} , thereby reversing the classical cognition that the voltage plateau is fixed for given positive and negative electrodes. This revolution enables an impressive discharge voltage plateau of 2.1 V in Zn full batteries. Resulted from the strong anchoring of polymeric backbone for SN and NMA to promote ion conduction ($3.94 \times 10^{-3} \text{ S cm}^{-1}$ at 25°C) and stabilize the interfacial reaction of Zn electrode, the symmetric batteries with 80% Zn utilization operate stably at 8.0 mA cm^{-2} for 1700 h, surpassing all non-aqueous and most aqueous zinc batteries. Thus, this work opens up a unique pathway to develop high-voltage, deep-reversible and durable solid-state Zn-based batteries and may apply to other metal-based batteries.

Methods

Materials

Buanedinitrile (SN; 98%, Alfa Aesar, America), N-methylacetamide (NMA; 99%, Alfa Aesar, America), zinc bis(trifluoromethylsulfonyl) imide ($\text{Zn}(\text{TFSI})_2$; $\geq 99\%$, Alfa Aesar, America), ethoxylated trimethylpropane triacrylate (ETPTA; average Mn-692 containing 100 ppm methyl ethyl hydroquinone (MEHQ) as a stabilize, Aladdin, China), azodiisobutyronitrile (AIBN; $\geq 99\%$, Aladdin, China), potassium ferrocyanide ($\text{K}_4\text{Fe}(\text{CN})_6$; $\geq 99\%$, Aladdin, China), ammonium metavanadate (NH_4VO_3 ; $\geq 99\%$, Aladdin, China), ammonium dihydrogen phosphate ($\text{NH}_4\text{H}_2\text{PO}_4$; $\geq 99\%$, Aladdin, China), sodium carbonate monohydrate ($\text{Na}_2\text{CO}_3 \cdot \text{H}_2\text{O}$; $\geq 99\%$, Aladdin, China), and sodium fluoride (NaF ; $\geq 99\%$, Aladdin, China) were purchased and used without further treatment.

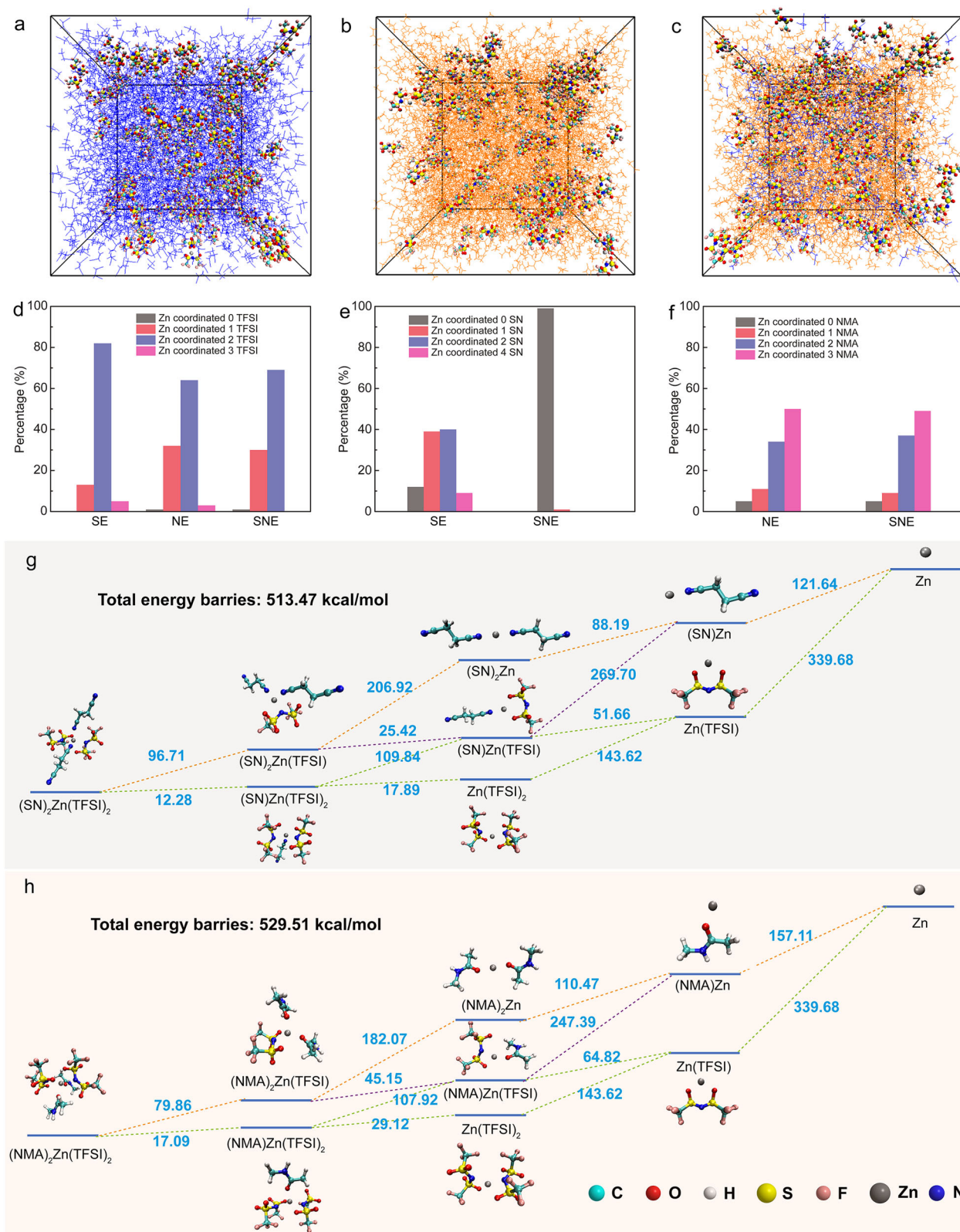


Fig. 6 | Theoretical calculation for the voltage-elevating of zinc batteries via solvation regulation. Snapshots of different eutectic electrolyte systems obtained by MD simulation at 298 K: **a** SE, **b** NE, and **c** SNE. The Zn²⁺ are presented by ball and stick model, while the wireframes stand for SN (blue) and NMA (orange), respectively. **d** Percentage of Zn²⁺ cations, which coordinate with different number of TFSI

anions in SE, NE, and SNE. **e** Percentage of Zn²⁺ cations, which coordinate with different number of SN molecules in SE and SNE. **f** Percentage of Zn²⁺ cations, which coordinate with different number of NMA molecules NE and SNE. **g, h** Diagram of the energy barriers (kcal/mol) during the step-by-step desolvation process of (SN)₂Zn(TFSI)₂ and (NMA)₂Zn(TFSI)₂.

The zinc foils ($\geq 99.99\%$, 20 μm thickness) were purchased from Guangdong Canrd New Energy Technology Co., LTD. (China) and used with washing of water and ethanol. The aluminum foil ($\geq 99.99\%$, 20 μm thickness), copper foil ($\geq 99.99\%$, 20 μm thickness) and titanium foil ($\geq 99.99\%$, 20 μm thickness) were purchased from Shenzhen Kejing Zhida Technology Co., LTD (China) and used without further treatment.

Synthesis of solid-state eutectic electrolytes (PSNE)

The solid butanedinitrile (SN) and N-methylacetamide (NMA) were mixed and stirred at 60 °C until completely melted, where the mass ratio of SN to NMA was 1:4. Subsequently, zinc bis(trifluoromethanesulfonyl)imide ($\text{Zn}(\text{TFSI})_2$) was added into above compounds at different molar concentrations (0.1 mol L⁻¹, 0.3 mol L⁻¹, 0.5 mol L⁻¹, 0.7 mol L⁻¹, and 1.0 mol L⁻¹), and the zinc salts were rapidly dissolved in the above solution and form a liquid eutectic electrolyte at 25 °C. In addition, the ethoxylated trimethylpropane triacrylate (ETPTA) was added to the eutectic electrolyte at 10% of the total mass of SN and NMA, and kept at 25 °C with homogeneous stirring for 2 h. After that, 0.5 wt% azodiisobutyronitrile (AIBN) was added to the above solution as initiator and stirred for 30 min to form a homogeneous precursor solution at 25 °C. Finally, the precursor solution was heated at 60 °C for 12 h to allow complete polymerization. The samples were named PSNE-1, PSNE-3, PSNE-5, PSNE-7 and PSNE-10 according to the different zinc salt concentrations. To achieve the in-situ polymerization of the solid electrolyte in the battery, the precursor solution was first injected into the battery as assembled with those conventional liquid electrolytes, and stood at 25 °C for 2 h to fully infiltrate the membranes and electrodes. Above experiments were carried out in a high-purity argon-filled glove box with less than 0.1 ppm O₂ and H₂O. Then, the battery was transferred to an oven to cure at 60 °C for 12 h to achieve thermally initiated in-situ polymerization of gel-type eutectic electrolyte. For comparison, solid electrolytes without NMA and SN, named PSE and PNE, respectively, were prepared by the same process described above.

Preparation of K_{1.6}Mn_{1.2}Fe(CN)₆ (MnHCF) and Na₃V₂(PO₄)₂O₂F (NVPOF)

MnHCF was prepared by a simple co-precipitation method³⁶. First, 50 mL of MnSO₄ solution (0.1 mol L⁻¹) was added dropwise to 100 mL of K₄Fe(CN)₆ (0.05 mol L⁻¹) solution, and the solution was stirred continuously during the dropwise addition. Then, the mixed solution was continued to stir magnetically in air (25 °C) for 12 h and washed with deionized water three times, and finally dried in an oven at 80 °C for 18 h to obtain the final product.

NVPOF was synthesized by a typical solvothermal method⁵⁰. First, NH₄VO₃ (0.242 g), NH₄H₂PO₄ (0.230 g), Na₂CO₃·H₂O (0.124 g) and NaF (0.042 g) were dissolved in 12 mL of deionized water in a molar ratio of 2:2:1:1 in air (25 °C). Afterwards, the above solution was added to 30 mL of DMF solvent and its pH was adjusted to 7 with HNO₃ in air (25 °C). Subsequently, the mixed solution was transferred to a 50 mL autoclave and reacted hydrothermally at 150 °C for 20 h. After the reaction, the products were collected by centrifugation and washed thoroughly with deionized water and ethanol, and finally dried at 100 °C for 10 h.

Materials Characterization

The morphology characterization of the samples was examined by scanning electron microscopy (SEM, SU8020). The crystal structure and phase identification were performed through X-ray diffraction analysis (XRD, D/max 2500). Information about molecular groups in the sample was characterized by Fourier transform infrared spectroscopy (Vertex 80), and the wavelength range tested was between 100 and 4000 cm⁻¹. Raman spectroscopy (alpha300R) with laser source of 532 nm was mainly used for the analysis of molecular interactions

between different components of solid state electrolytes, and the test range is 100–4000 cm⁻¹. A thermogravimetric analyzer (STA 449 F5) was used to characterize the thermal effects of the solid state electrolytes.

Electrochemical Characterization

The electrochemical workstation (CHI 760E, Shanghai Chenhua) was employed to perform cyclic voltammetry (CV) tests on various batteries under ambient air conditions at 25 °C, aiming to investigate the electrochemical behavior of electrode materials. Additionally, the electrochemical impedance spectra (EIS) measurements were conducted to elucidating the resistance characteristics inside the batteries (25 °C to 100 °C). A potential amplitude of 5 mV was applied, with 12 data points collected per frequency decade across 0.01 Hz to 100 kHz. Prior to measurements, an open-circuit voltage was maintained for 5 minutes. For galvanostatic charge/discharge (GCD) measurements of symmetrical batteries and full batteries, the 2032-type coin-cells (LAND, CT2001A) were assembled with Pure Zn and ZnSnF@Zn as negative electrode in solid eutectic electrolytes, and the electrochemical tests were conducted in air (25 ± 1 °C). To fabricate the positive electrode, active materials, conductive carbon black (Super P; $\geq 99\%$, Guangdong Canrd New Energy Technology Co., LTD.; China), and polyvinylidene fluoride (PVDF; $\geq 99.5\%$, PVDF5130, Guangdong Canrd New Energy Technology Co., LTD.; China) binder was mixed in N-Methylpyrrolidone (NMP; 99%, Guangdong Canrd New Energy Technology Co., LTD.; China) with a mass ratio of 8:1:1 in a dry air atmosphere (25 °C), and then the slurry was cast on the aluminum foil via hand coating and dried at a vacuum oven at 80 °C for 12 h. The precursor solution was first injected into the battery as assembled with those conventional liquid electrolytes, and stood at around 25 °C for 2 h to fully infiltrate the membrane and electrodes. Then, the battery was cured at 60 °C for 12 h to complete thermally initiated in-situ polymerization. The volume of the precursor solution used in coin cell assembly was 120 μL , which was loaded onto the membranes (GF-A, Whatman, 1.8 cm diameter, 0.26 mm thickness, 53 g/m² areal density, 1.6 μm average pore size). Furthermore, the pouch batteries were applied to assess their practical application, and the assembly process went through sequentially the stamping forming of aluminum plastic film, stacking of electrodes and membranes (GF-A, Whatman, 5.1 cm × 4.1 cm, 0.26 mm thickness, 53 g/m² areal density, 1.6 μm average pore size), fixing of the tabs, top and side seals, electrolyte injection, venting and final seals in a dry room (with a dew point of 15 °C), which were carried out in a high-purity argon-filled glove box with less than 0.1 ppm O₂ and H₂O. The size of the positive and negative electrode pieces were approximately 5 cm × 4 cm, and electrolyte (1.2 mL–1.5 mL) goes through thermally initiated polymerization after assembling the pouch cell. During cycling, the pouch cells were subjected to a pressure of 101.325 kPa and a temperature of 25 ± 1 °C, respectively. Besides, the active material mass loading on the positive electrode pieces of both coin and pouch cells was in the range of 2.0 to 2.5 mg cm⁻². The thickness of both as-polymerized PSNE electrolyte and zinc metal electrode is 20 μm .

First-principles calculations (DFT)

The theoretical calculations were performed via the Gaussian 16 suite of programs⁵¹. The geometric configurations of the molecular systems and Zn²⁺-TSF⁻ complexes were computationally optimized using B3LYP-D3BJ/def2-SVP theoretical method. Subsequent vibrational frequency analysis at the same computational level confirmed the absence of imaginary frequencies, guaranteeing stable energy minima on the potential energy surface. Thermodynamic stability was evaluated through binding energy calculations for the coordination

complexes. Quantum chemical investigations further probed frontier molecular orbital distributions, including HOMO and LUMO energy levels. Spatial representations of molecular electrostatic potentials (MESP) and orbital distributions were visualized using the Visual Molecular Dynamics (VMD) program, which generated color-mapped iso-surface diagrams for enhanced interpretability⁵².

Molecular dynamics simulation (MD)

MD simulations were performed on the electrolytes using Gromacs 2019.4 package^{53,54}. General Amber force fields parameters and RESP charges were used for all the molecules. The force field parameters for Zn(TFSI)₂, SN, and NMA were derived using the SobTop computational platform. Detailed parameters for the simulated electrolyte systems are summarized in Supplementary Table S3. To establish equilibrium configurations, NPT ensemble molecular dynamics simulations were executed at 298 K for a 100 ns duration, with structural equilibration confirmed through analysis of the final 20 ns trajectory. Molecular configurations were visualized and analyzed using the VMD software suite for spatial representation.

The DFT calculation was performed with the Gaussian 16 package using the hybrid B3LYP functionals. The 6-31 + G* basis set was used for C, H, O, N, S and F elements, and LanL2DZ pseudo potential basis set for Zn element.

Data availability

The detailed data generated in this study are provided in the Source Data file. Source data are provided with this paper.

References

- Kalnaus, S., Dudney, N. J., Westover, A. S., Herbert, E. & Hackney, S. Solid-state batteries: the critical role of mechanics. *Science* **381**, eabg5998 (2023).
- Wang, W. et al. Flexible quasi-solid-state aqueous zinc-ion batteries: design principles, functionalization strategies, and applications. *Adv. Energy Mater.* **13**, 2300250 (2023).
- Hu, E. & Yang, X.-Q. Rejuvenating zinc batteries. *Nat. Mater.* **17**, 480–481 (2018).
- Chen, Z. et al. Polymeric single-ion conductors with enhanced side-chain motion for high-performance solid zinc-ion batteries. *Adv. Mater.* **34**, 2207682 (2022).
- Qiu, H. et al. Eutectic crystallization activates solid-state zinc-ion conduction. *Angew. Chem. Int. Ed.* **61**, e202113086 (2022).
- Chen, Z. et al. Grafted MXene/polymer electrolyte for high performance solid zinc batteries with enhanced shelf life at low/high temperatures. *Energy Environ. Sci.* **14**, 3492–3501 (2021).
- Ge, H. et al. Critical challenges and solutions: quasi-solid-state electrolytes for zinc-based batteries. *Energy Environ. Sci.* **17**, 3270–3306 (2024).
- Leng, K. et al. A safe polyelectrolytic hydrogel electrolyte for long-life quasi-solid state zinc metal batteries. *Adv. Funct. Mater.* **30**, 2001317 (2020).
- Su, L. et al. Gyroid liquid crystals as quasi-solid-state electrolytes toward ultrastable zinc batteries. *ACS Nano* **18**, 7633–7643 (2024).
- Qiu, T. et al. Rapidly synthesized single-ion conductive hydrogel electrolyte for high-performance quasi-solid-state zinc-ion batteries. *Angew. Chem. Int. Ed.* **135**, e202312020 (2023).
- Chen, Z. et al. Polymer hetero-electrolyte enabled solid-state 2.4-V Zn/Li hybrid batteries. *Nat. Commun.* **15**, 3748 (2024).
- Ki, C. et al. Completely activated and phase-transformed KFeMnHCF for Zn/K hybrid batteries with 14500 cycles by an OH-rich hydrogel electrolyte. *Adv. Mater.* **36**, 2304878 (2024).
- Liu, Z. et al. A flexible solid-state aqueous zinc hybrid battery with flat and high-voltage discharge plateau. *Adv. Energy Mater.* **9**, 1902473 (2019).
- Li, J. et al. Multifunctional dual-metal-salt derived ternary eutectic electrolyte for highly reversible zinc ion battery. *Adv. Funct. Mater.* **34**, 2402186 (2024).
- Miao, C. L. et al. Spatially confined engineering toward deep eutectic electrolyte in metal-organic framework enabling solid-state zinc-ion batteries. *Angew. Chem. Int. Ed.* **63**, e202410208 (2024).
- Zhang, C., Zhang, L. & Yu, G. Eutectic electrolytes as a promising platform for next-generation electrochemical energy storage. *Acc. Chem. Res.* **53**, 1648–1659 (2020).
- Song, X. et al. Ternary eutectic electrolyte-assisted formation and dynamic breathing effect of the solid-electrolyte interphase for high-stability aqueous magnesium-ion full batteries. *J. Am. Chem. Soc.* **146**, 7018–7028 (2024).
- Gao, Y. et al. Molecular engineering enabled stable deep eutectic amide-based electrolyte for high-temperature lithium-metal batteries. *ACS Energy Lett.* **9**, 3931–3938 (2024).
- Chen, F. et al. Direct crystallization of deep eutectic solvent into solid-state electrolyte for magnesium metal batteries. *J. Power Sources* **611**, 234780 (2024).
- Miao, C.-L. et al. Spatially confined engineering toward deep eutectic electrolyte in metal-organic framework enabling solid-state zinc-ion batteries. *Angew. Chem. Int. Ed.* **63**, e202410208 (2024).
- Wan, J. et al. Hydrated eutectic electrolyte induced bilayer interphase for high-performance aqueous Zn-ion batteries with 100 °C wide-temperature range. *Adv. Mater.* **36**, 2310623 (2024).
- Li, C. et al. Enabling selective zinc-ion intercalation by a eutectic electrolyte for practical anodeless zinc batteries. *Nat. Commun.* **14**, 3067 (2023).
- Lu, X. et al. Ultra-stable zinc metal anodes at -20 °C through eutectic solvation sheath in chlorine-functionalized eutectic electrolytes with 1, 3-dioxolane. *Angew. Chem. Int. Ed.* **135**, e202307475 (2023).
- Niu, B. et al. Polymers for aqueous zinc-ion batteries: from fundamental to applications across core components. *Adv. Energy Mater.* **14**, 2303967 (2024).
- Liu, Z., Sun, B., Zhang, Y., Zhang, Q. & Fan, L. Polymer-adjusted zinc anode towards high-performance aqueous zinc ion batteries. *Prog. Polym. Sci.* **152**, 101817 (2024).
- Zhong, Y. et al. Triple-function hydrated eutectic electrolyte for enhanced aqueous zinc batteries. *Angew. Chem. Int. Ed.* **62**, e202310577 (2023).
- Cheng, M. et al. Anions-in-colloid hydrated deep eutectic electrolyte for high reversible zinc metal anodes. *Angew. Chem. Int. Ed.* **63**, e202410210 (2024).
- Wang, H. et al. A shuttle-free solid-state Cu-Li battery based on a sandwich-structured electrolyte. *Angew. Chem. Int. Ed.* **135**, e202214117 (2022).
- Ehara, M. et al. Gaussian 16, Revision A. 03. Gaussian, Inc., Wallingford, CT, (2016).
- Ling, W. et al. Ion sieve interface assisted zinc anode with high zinc utilization and ultralong cycle life for 61 Wh/kg mild aqueous pouch battery. *ACS Nano* **18**, 5003–5016 (2024).
- Tang, D. et al. Switching hydrophobic interface with ionic valves for reversible zinc batteries. *Adv. Mater.* **36**, 2406071 (2024).
- Zheng, Z. et al. An extended substrate screening strategy enabling a low lattice mismatch for highly reversible zinc anodes. *Nat. Commun.* **15**, 753 (2024).
- Yang, M. et al. The Construction of anion-induced solvation structures in low-concentration electrolyte for stable zinc anodes. *Angew. Chem. Int. Ed.* **63**, e202400337 (2024).

34. Li, Q. et al. High-voltage K/Zn dual-ion battery with 100,000-cycles life using zero-strain ZnHCF cathode. *Energy Storage Mater.* **42**, 715–722 (2021).
35. Guo, J. Z. et al. High-energy/power and low-temperature cathode for sodium-ion batteries: in situ XRD study and superior full-cell performance. *Adv. Mater.* **29**, 1701968 (2017).
36. Li, Q., Ma, K., Yang, G. & Wang, C. High-voltage non-aqueous Zn/ $K_{1.6}Mn_{1.2}Fe(CN)_6$ batteries with zero capacity loss in extremely long working duration. *Energy Storage Mater.* **29**, 246–253 (2020).
37. Wang, F. et al. Quantifying and suppressing proton intercalation to enable high-voltage Zn-ion batteries. *Adv. Energy Mater.* **11**, 2102016 (2021).
38. Zhao, Q. et al. High-capacity aqueous zinc batteries using sustainable quinone electrodes. *Sci. Adv.* **4**, eaao1761 (2018).
39. Zhu, Y. et al. High areal capacity and long cycle life flexible mild quasi-solid-state Ag-Zn battery with dendrite-free anode. *Energy Environ. Mater.* **7**, e12493 (2024).
40. Pan, H. et al. Reversible aqueous zinc/manganese oxide energy storage from conversion reactions. *Nat. Energy* **1**, 1–7 (2016).
41. Qiu, N. et al. Toward a high-performance aqueous zinc ion battery: potassium vanadate nanobelts and carbon enhanced zinc foil. *Nano Lett.* **21**, 2738–2744 (2021).
42. Yang, Q. et al. Activating C-coordinated iron of iron hexacyanoferrate for Zn hybrid-ion batteries with 10000-cycle lifespan and superior rate capability. *Adv. Mater.* **31**, 1901521 (2019).
43. Ma, L. et al. Achieving high-voltage and high-capacity aqueous rechargeable zinc ion battery by incorporating two-species redox reaction. *Adv. Energy Mater.* **9**, 1902446 (2019).
44. Cui, H. et al. High-voltage organic cathodes for zinc-ion batteries through electron cloud and solvation structure regulation. *Angew. Chem. Int. Ed.* **134**, e202203453 (2022).
45. Huang, M., Meng, J., Huang, Z., Wang, X. & Mai, L. Ultrafast cation insertion-selected zinc hexacyanoferrate for 1.9 V K-Zn hybrid aqueous batteries. *J. Mater. Chem. A* **8**, 6631–6637 (2020).
46. Clement, O., Rapko, B. & Hay, B. Structural aspects of metal-amide complexes. *Coord. Chem. Rev.* **170**, 203–243 (1998).
47. Geng, L. et al. Eutectic electrolytes in advanced metal-ion batteries. *ACS Energy Lett.* **7**, 247–260 (2022).
48. Huang, Z. et al. Manipulating anion intercalation enables a high-voltage aqueous dual ion battery. *Nat. Commun.* **12**, 3106 (2021).
49. Cui, H. et al. High-voltage organic cathodes for zinc-ion batteries through electron cloud and solvation structure regulation. *Angew. Chem. Int. Ed.* **61**, e202203453 (2022).
50. Dong, Y. et al. Nonaqueous electrolyte with dual-cations for high-voltage and long-life zinc batteries. *J. Mater. Chem. A* **8**, 3252–3261 (2020).
51. Frisch, M. et al. Gaussian 16 Revision. A.03, Gaussian Inc., Wallingford, CT (2016).
52. Humphrey, W., Dalke, A. & Schulten, K. VMD: Visual molecular dynamics. *J. Mol. Graph.* **14**, 33–38 (1996).
53. Abraham, M. J. et al. GROMACS: High performance molecular simulations through multi-level parallelism from laptops to supercomputers. *SoftwareX* **1**, 19–25 (2015).
54. Van Der Spoel, D. et al. GROMACS: fast, flexible, and free. *J. Comput. Chem.* **26**, 1701–1718 (2005).
55. Han, D. et al. A non-flammable hydrous organic electrolyte for sustainable zinc batteries. *Nat. Sustain.* **5**, 205–213 (2021).
56. Ming, F. et al. Co-solvent electrolyte engineering for stable anode-free zinc metal batteries. *J. Am. Chem. Soc.* **144**, 7160–7170 (2022).
57. Yu, H. et al. Confining Sn nanoparticles in interconnected N-doped hollow carbon spheres as hierarchical zincophilic fibers for dendrite-free Zn metal anodes. *Sci. Adv.* **8**, eabm5766 (2022).
58. Zhao, R. et al. Lanthanum nitrate as aqueous electrolyte additive for favourable zinc metal electrodeposition. *Nat. Commun.* **13**, 3252 (2022).
59. Dong, D., Wang, T., Sun, Y., Fan, J. & Lu, Y.-C. Hydrotropic solubilization of zinc acetates for sustainable aqueous battery electrolytes. *Nat. Sustain.* **6**, 1474–1484 (2023).
60. Ilyas, F. et al. Empowering Zn electrode current capability along interfacial stability by optimizing intrinsic safe organic electrolytes. *Angew. Chem. Int. Ed.* **62**, e202215110 (2023).
61. Xu, Y.-T. et al. Remodeling zinc deposition via multisite zincophilic chlorophyll for powerful aprotic zinc batteries. *Nano Lett.* **23**, 5722–5730 (2023).
62. Cai, X. et al. A layer-by-layer self-assembled bio-macromolecule film for stable zinc anode. *Adv. Mater.* **36**, 2306734 (2024).
63. Liu, C. et al. Electrochemical hydrophobic tri-layer interface rendered mechanically graded solid electrolyte interface for stable zinc metal anode. *Angew. Chem. Int. Ed.* **63**, e202318063 (2024).
64. Liu, L. et al. Electric double layer regulator design through a functional group assembly strategy towards long-lasting zinc metal batteries. *Angew. Chem. Int. Ed.* **63**, e202405209 (2024).
65. Lyu, H. et al. Electric double layer oriented eutectic additive design toward stable Zn anodes with a high depth of discharge. *Adv. Mater.* **36**, 2400976 (2024).
66. Ma, C. et al. Dual-parasitic effect enables highly reversible Zn metal anode for ultralong 25,000 cycles aqueous zinc-ion batteries. *Nano Lett.* **24**, 4020–4028 (2024).
67. Ma, L. et al. Engineering a zinc anode interphasial chemistry for acidic, alkaline and non-aqueous electrolytes. *Energy Environ. Sci.* **17**, 2468–2479 (2024).
68. Yang, S. et al. Regulating the electrochemical reduction kinetics by the steric hindrance effect for a robust Zn metal anode. *Energy Environ. Sci.* **17**, 1095–1106 (2024).
69. Zhang, X. et al. Single [0001]-oriented zinc metal anode enables sustainable zinc batteries. *Nat. Commun.* **15**, 2735 (2024).
70. Zhou, K., Liu, G., Yu, X., Li, Z. & Wang, Y. Carbonate ester-based electrolyte enabling rechargeable Zn battery to achieve high voltage and high Zn utilization. *J. Am. Chem. Soc.* **146**, 9455–9464 (2024).
71. Zhou, S. et al. Zinc-ion anchor induced highly reversible Zn anodes for high performance Zn-ion batteries. *Angew. Chem. Int. Ed.* **63**, e202403050 (2024).
72. Zhu, J. et al. The construction of binary phase electrolyte interface for highly stable zinc anodes. *Adv. Mater.* **36**, 2304426 (2024).
73. Zhu, Q. et al. Selective shielding of the (002) plane enabling vertically oriented zinc plating for dendrite-free zinc anode. *Adv. Mater.* **36**, 2308577 (2024).

Acknowledgements

This research was supported by the Talent Recruitment Project of Guangdong Province (Grant No. 2019QN01C883), the Shenzhen Science and Technology Program (Grant No. RCJC20231211090017038, JCYJ20220818102402004), the Shenzhen Sauvage Nobel Laureate Laboratory for Smart Materials, the Science and Technology Innovation Program of Hunan Province (Grant No. 2023RC3154), the Excellent Youth Program of the Education Department of Hunan Province (Grant No. 23B0221), the Natural Science Foundation of Hunan Province of China (Grant No. 2024JJ6232) and the Key Program of the Education Department of Hunan Province (Grant No. 23A0188).

Author contributions

Y.H. and W.L. conceived the idea and revised the manuscript. W.L. performed data analysis, wrote the original draft, and designed/conducted the experiments and computations in collaboration with X.W.W., X.X.Z., and J.X. Figure preparation was completed by W.L. and F.N.M. Y.H. supervised the entire manuscript.

Competing interests

The authors declare no competing interests.

Additional information

Supplementary information The online version contains supplementary material available at <https://doi.org/10.1038/s41467-025-60125-5>.

Correspondence and requests for materials should be addressed to Yan Huang.

Peer review information *Nature Communications* thanks Guoyong Huang, and the other, anonymous, reviewer(s) for their contribution to the peer review of this work. A peer review file is available.

Reprints and permissions information is available at <http://www.nature.com/reprints>

Publisher's note Springer Nature remains neutral with regard to jurisdictional claims in published maps and institutional affiliations.

Open Access This article is licensed under a Creative Commons Attribution-NonCommercial-NoDerivatives 4.0 International License, which permits any non-commercial use, sharing, distribution and reproduction in any medium or format, as long as you give appropriate credit to the original author(s) and the source, provide a link to the Creative Commons licence, and indicate if you modified the licensed material. You do not have permission under this licence to share adapted material derived from this article or parts of it. The images or other third party material in this article are included in the article's Creative Commons licence, unless indicated otherwise in a credit line to the material. If material is not included in the article's Creative Commons licence and your intended use is not permitted by statutory regulation or exceeds the permitted use, you will need to obtain permission directly from the copyright holder. To view a copy of this licence, visit <http://creativecommons.org/licenses/by-nc-nd/4.0/>.

© The Author(s) 2025